

High Resolution VLA Radio Observations of the Boomerang Pulsar Wind Nebula

PAUL C. W. LAI ^{1,2}, C.-Y. NG ^{1,3} AND SHUMENG ZHANG ^{1,3}

¹*Department of Physics, The University of Hong Kong, Pokfulam Road, Hong Kong*

²*Mullard Space Science Laboratory, University College London, Holmbury St Mary, Surrey RH5 6NT, United Kingdom*

³*Hong Kong Institute for Astronomy and Astrophysics, The University of Hong Kong, Pokfulam Road, Hong Kong*

ABSTRACT

We present a radio polarimetric study of the Boomerang pulsar wind nebula G106.65+2.96 with VLA observations at the 6 GHz band. Our high-resolution image discovers new small-scale features in the nebula, including an elliptical core of $40'' \times 20''$ surrounding the central pulsar and a $2'$ -long arc wrapping around the core in the north. The latter shows a clear gap from the core, and it consists of a bright lobe in the northwest and a tongue-like structure in the northeast. These could be resulting from the pulsar wind interaction with the environment. Our polarization measurement reveals a highly ordered magnetic field with toroidal geometry. The small scale features are all highly linearly polarized. In particular, the lobe has a polarization fraction of $\sim 60\%$, close to the synchrotron limit. This is also much higher than the value measured at a lower frequency, implying significant depolarization. We show that this can be explained by Faraday rotation in the nebula, and we constructed a simple 3D model accordingly to infer a magnetic field strength of $\sim 50\text{--}105 \mu\text{G}$.

Keywords: Pulsar wind nebulae (2215) — Supernova remnants (1667) — Galactic radio sources (571) — Very Large Array (1766) — Polarimetry (1278) — Interstellar medium (847)

1. INTRODUCTION

A pulsar is a rapidly rotating, highly magnetized neutron star produced in a supernova explosion at the end stage of massive stellar evolution. As an analog to a rotating magnet, a pulsar can create a huge electric potential around it. This accelerates charged particles to relativistic speeds, driving a magnetized outflow known as a pulsar wind (see [E. Amato 2024](#), for a review). The wind mainly composes of electrons and positrons. When these particles interact with the surrounding medium, either the interstellar medium or the supernova remnant (SNR), a termination shock is formed, and they are further accelerated to ultra-relativistic energies at the shock. The high energy particles then inflate a synchrotron bubble emitting from radio to X-ray bands. Such a structure is called a pulsar wind nebula (PWN).

The fast rotation of a pulsar wraps its magnetic field lines, making them nearly toroidal before reaching the termination shock ([I. Contopoulos et al. 1999](#)). Downstream of the shock, the plasma flow becomes turbulent and a poloidal B -field component emerges ([O. Porth et al. 2014](#); [B. Olmi et al. 2016](#); [B. Olmi & N. Bucciantini 2023](#)). Observationally, this can be tested with polarimetric measurements, since PWN emission is dominated

by synchrotron emission which is highly linearly polarized and the polarization angle can reveal the local magnetic field direction at the emission site. Previous observations of PWNe show a vast variety of magnetic field configurations, including a radial field (e.g., DA 495 and G21.5–0.9; [R. Kothes et al. 2008](#); [P. C. W. Lai et al. 2022](#)), a large-scale toroidal field (e.g., Vela; [R. Dodson et al. 2003](#)), an elongated field aligned with the pulsar spin axis (e.g., 3C58; [W. Reich 2002](#)), and other complex structures (e.g., the Crab and G292.0+1.8; [M. F. Bietenholz & P. P. Kronberg 1990](#); [B. M. Gaensler & B. J. Wallace 2003](#)). The diverse behavior is very difficult to be explained by a unified picture.

The Boomerang (G106.6+2.9 or G106.65+2.96) is a middle-aged PWN located at the tip of the associated SNR G106.3+2.7 ([R. Kothes et al. 2001](#)). It is powered by pulsar J2229+6114 which has spin period $P = 51.6$ ms, spin-down rate $\dot{P} = 7.83 \times 10^{-14}$, surface magnetic field $B = 2.0 \times 10^{12}$ G, spin-down luminosity $\dot{E} = 2.2 \times 10^{37}$ ergs $^{-1}$, and characteristic age $\tau_c = 10.5$ kyr ([J. P. Halpern et al. 2001](#)). In the radio band, the PWN shows an arc-like overall morphology of $\sim 3'$ long that resembles a boomerang ([R. Kothes et al. 2006](#)). This shape is highly unusual among PWNe, as the emission is found only on one side of pulsar, and the

peak is significantly offset from the pulsar location. This is believed to be resulting from crushing of the nebula by the supernova reverse shock 3.9 kyr ago (R. Kothes et al. 2006). The X-ray image of the Boomerang reveals a drastically different structure: the radio core and tongue are not detected, but there is an X-ray arc of $\sim 20''$ with a jet-like feature surrounding the pulsar (J. P. Halpern et al. 2001), which is interpreted as the toroidal termination shock (C. Y. Ng & R. W. Romani 2004, 2008). Beyond that, there is very faint, large-scale diffuse X-ray emission extending south (C. Ge et al. 2021). Such morphology indicates that the X-ray nebula could be a revived or reborn PWN after the passage of the SNR reverse shock.

The Boomerang has drawn much attention in gamma-ray studies lately. Ultra-high energy photons up to 570 TeV are detected in the direction of the SNR, suggesting that this is a PeVatron—an astrophysical source that can accelerate particles up to PeV energies (Z. Cao et al. 2021). The exact production site and mechanism of the gamma-rays are still under debate. Previous radio observations discovered a dense HI shell surrounding the Boomerang (R. Kothes et al. 2001), which provides some support for a hadronic origin (C. Ge et al. 2021; C. Yang et al. 2022), but a leptonic origin from pulsar wind is also possible (see S. Liu et al. 2020).

Single-dish radio measurements found a spectral break for the Boomerang around 4.3 GHz (R. Kothes et al. 2006). This is rather uncommon. If interpreted as the synchrotron cooling break, the magnetic field strength of the Boomerang would be 2.6 mG, much stronger than the typical values of 10–100 μ G (e.g., Y. K. Ma et al. 2016; Y. H. Liu et al. 2023). Later studies argue for a much weaker field from 3 μ G to 140 μ G based on pressure estimate (R. A. Chevalier & S. P. Reynolds 2011) and modeling of the broadband spectrum from radio to gamma-rays (X.-H. Liang et al. 2022; I. Pope et al. 2024). This implies that the 4.3 GHz break could be intrinsic instead of due to cooling. Radio polarization measurements found a toroidal configuration for the projected B -field, similar to that of the Vela PWN (R. Dodson et al. 2003). However, the distribution of rotation measure (RM) in the nebula prefers a radial field instead (R. Kothes et al. 2006).

In this paper, we revisit the Boomerang PWN using high resolution radio observations taken with the Karl G. Jansky Very Large Array (VLA) to further investigate the nebular magnetic field structure. We note that in the literature there are various distance estimates for this source, ranging from 0.8 to 12 kpc (see I. Pope et al. 2024, and references therein). We adopt 0.8 kpc in this work as this best explains the PWN and SNR morphol-

ogy in radio (R. Kothes et al. 2001, 2006). This paper is organized as following: the observation details and imaging method are described in Section 2 and the results are presented in Section 3. In Section 4, we present an interpretation of the PWN morphology, and we model the magnetic field strength and structure based on the observational results. Finally, we summarize our findings in Section 5.

2. OBSERVATION AND DATA REDUCTION

The Boomerang PWN was observed with the Karl G. Jansky Very Large Array (hereafter: VLA) in the C band (4–8 GHz). The observations were taken in the B array configuration on 2017 Nov 3, 12, and 21, with 230 min total on-source time and in the C array configuration on 2021 Jul 11, with 60 min on-source time. We combined all data to produce high-resolution images. The u - v coverage and calibrators of the observations are listed in Table 1. All data reduction was done using the Common Astronomical Software Application (CASA) version 6.2.1 (CASA Team et al. 2022). The data were first processed with the pipeline for preliminary flaggings and standard calibrations. We then further examined and flagged the remaining suspected RFI signals, and re-calibrated the data manually. The polarization calibration was also performed manually at this stage.

All the images were generated and cleaned using the CASA task `tclean`. To optimize between sensitivity and resolution, we chose the Briggs weighting algorithm with `robust = 1.0` for all the images. The Stokes I, Q, and U maps at 6 GHz were produced by combining all the available data using the full bandwidth. Since we mainly focus on the extended emission of the PWN, we applied a Gaussian uv -taper of 80 k λ to effectively smooth the images and increase sensitivity towards extended emission. The cleaned images are restored and then corrected for primary beam sensitivity. The linear polarization intensity (PI) map is obtained by combining the Stokes Q and U maps ($PI = \sqrt{Q^2 + U^2}$), with the Ricean bias corrected (J. F. C. Wardle & P. P. Kronberg 1974). Our final Stokes I and PI images at 6 GHz have a beam size of FWHM $2''.3 \times 1''.8$ and rms noise of 5μ Jy beam $^{-1}$. The latter is compatible with the theoretical estimate.

Forming images using the entire 4 GHz bandwidth improves the u - v coverage, but this could lead to slight bandwidth depolarization. Previous studies found that the rotation measure (RM) of the nebula is around -200 rad m^{-2} (R. Kothes et al. 2006), therefore combining the 4–8 GHz data would cause $\sim 7\%$ depolar-

Table 1. VLA observations used in this study

Observing date	2017 Nov 3	2017 Nov 12	2017 Nov 21	2021 Jul 11
VLA array configuration	B	B	B	C
Center frequency (GHz)	6.0	6.0	6.0	6.0
Bandwidth (GHz)	4.0	4.0	4.0	4.0
On-source time (min)	40	95	95	60
Baseline (km)	0.18–9.9	0.12–10.3	0.24–10.7	0.03–3.1
u - v coverage ($k\lambda$)	2.5–260	2–270	3.5–280	0.42–82
Flux calibrator	3C138	3C286	3C138	3C138
Phase calibrator	J2148+6107	J2148+6107	J2148+6107	J2148+6107
Polarization angle calibrator	3C138	3C286	3C138	3C138
Polarization leakage calibrator	J2355+4950	J1407+2827	J2355+4950	J2355+4950

ization⁴. We argue that this level is acceptable, as it is comparable to the measurement uncertainties of our observations.

To correct for foreground Faraday rotation, we divided the full band into four 1 GHz-wide subbands to generate the polarization position angle (PA) maps. The same imaging and deconvolution procedures as above were employed, but we slightly reduced the spatial resolution to boost the signal-to-noise ratio, by employing a uv -taper of $40 k\lambda$ and a restoring beam of FWHM $5''.0 \times 5''.0$. The observed PA of the polarization vectors is calculated from the Stokes Q and U maps as $PA = \frac{1}{2} \arctan(U/Q)$. A linear fit to PA values with respect to the square of wavelength (λ^2) gives the RM map and the intrinsic PA. We discard any fits that have RM uncertainty over 45 rad m^{-2} or intrinsic PA uncertainty over 15° , or if the total intensity is fainter than $15 \mu\text{Jy beam}^{-1}$ at 6 GHz.

The same subband images in Stokes I are used to perform spectral tomography (see [B. M. Gaensler & B. J. Wallace 2003](#), and references therein) to determine the spectral index of the small scale features in the Boomerang. We scaled the subband intensity maps at 4.5 and 7.5 GHz with trial spectral indices α_t to form difference images. When a feature blends into the background, α_t then gives its spectral index.

3. OBSERVATION RESULTS

3.1. Source structure

Figure 1a shows the 6 GHz total intensity map of the Boomerang formed using the full bandwidth of 4 GHz.

Our high resolution images reveal, for the first time, the detailed structure of the PWN. We discover several bright radio features embedded in diffuse emission. In the inner PWN, PSR J2229+6114 is not detected in our observations, but there is a compact radio nebula, which we call the “core”, near the pulsar position. It has an elliptical shape of $40'' \times 20''$ lying along the northeast-southwest direction and has mean brightness temperature of $\sim 0.15 \text{ K}$ at 6 GHz. The pulsar is located at the southeastern edge of the core. Further southeast of the pulsar, there exists a subluminescent zone of $25'' \times 12''$ without obvious radio emission. At the northern tip of the core, there is a hint of extended emission towards southeast. If confirmed, then the overall morphology of the core would also resemble a mini boomerang instead of merely elliptical.

In the north, there is a semicircular arc-like feature that encloses the entire core. It has a width of $20''$ – $30''$ with a sharp boundary in the north. Its morphology closely follows that of the core, and there is a gap of $\sim 30''$ between them (see Fig. 1c). The arc can be roughly divided into two parts. The northwestern part, which we refer to as the “lobe”, is about $120'' \times 40''$ in size, and it contains the peak emission of the radio PWN with a brightness temperature of up to $\sim 0.3 \text{ K}$ at 6 GHz. The northeastern part of the arc is significantly fainter and smaller ($80'' \times 20''$) and is called the “tongue” in a previous study ([R. Kothes et al. 2006](#)). All these bright features are embedded in faint diffuse emission that fills the gap between the arc and the core. It further extends southwest in the general direction of the orientation core. The emission fades and becomes undetectable at $3.5'$ from the pulsar.

In Figure 1d we show an X-ray image taken with the *Chandra X-ray Observatory* for comparison ([J. P. Halpern et al. 2001](#)). The X-ray PWN exhibits a clear

⁴ The bandwidth depolarization fraction is given by $f_{\text{depol}} = 1 - \sin(\Delta\theta)/\Delta\theta$, where $\Delta\theta = 2\text{RM}c^2\Delta\nu/\nu_c^3$, ν_c is the center frequency and $\Delta\nu$ is the bandwidth.

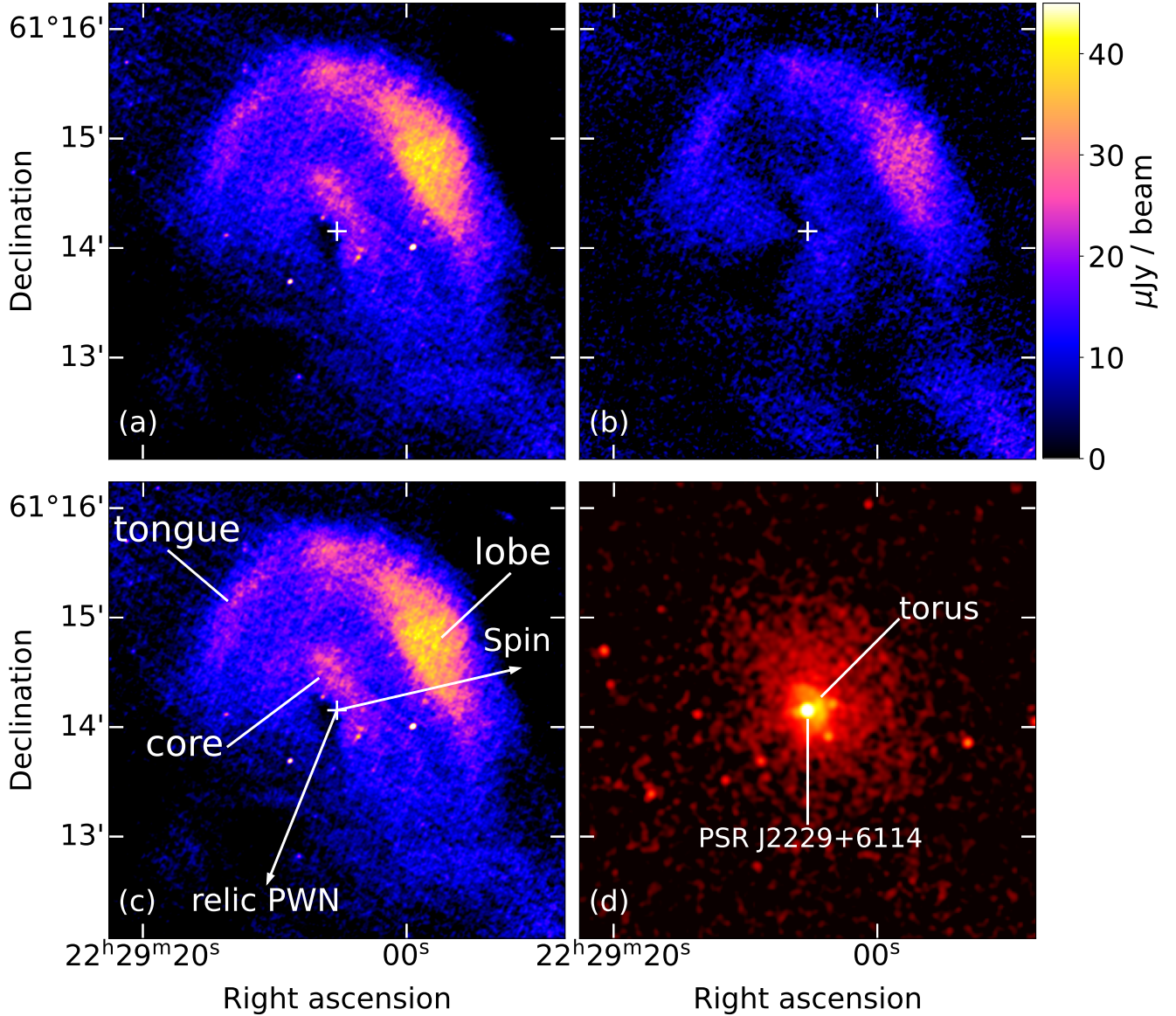


Figure 1. (a) VLA total intensity and (b) linear polarized intensity maps of the Boomerang PWN at 6 GHz. The white crosses mark the position of PSR J2229+6114. The radio images have a beam size of $2''.3 \times 1''.8$ FWHM and rms noise of 5 mJy beam^{-1} . (c) same as (a) with different PWN features labeled. The arrow pointing west shows the pulsar spin axis direction inferred from the X-ray PWN (C. Y. Ng & R. W. Romani 2004). The arrow pointing southeast indicates the direction to the relic PWN (R. Kothes et al. 2001). (d) Exposure corrected *Chandra* X-ray image of the same field, showing the central pulsar J2229+6119 and the surrounding torus.

torus structure with a $\sim 0.5'$ diameter (C. Y. Ng & R. W. Romani 2004, 2008), which is significantly smaller than the radio core and has a different orientation. This is surrounded by faint diffuse X-ray emission of approximately circular shape with $\sim 2'$ diameter. The emission fills in the gap between the radio core and the arc. Its surface brightness drops radially outward and becomes undetectable near the inner edge of the radio arc.

3.2. Polarization

The PI map of the Boomerang is shown in Figure 1b. The polarized emission well follows the total intensity. The core, the lobe, and the tongue have high polarized fractions (PF) of $\sim 57\%$, $\sim 60\%$ and $\sim 45\%$, respectively, and the average PF of the overall PWN is $\sim 50\%$. These values are higher than the previously reported value at a similar frequency ($37 \pm 5\%$ at 4.85 GHz; R. Kothes et al. 2006), likely due to reduced beam depolarization in our high-resolution image.

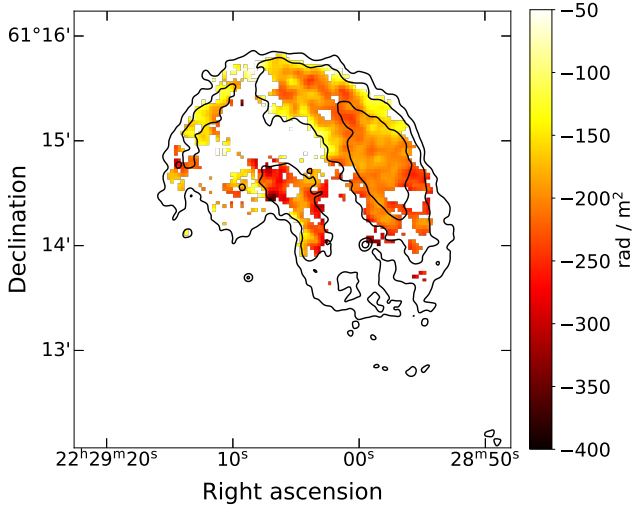


Figure 2. RM map of the Boomerang PWN overlaid with the 6 GHz total intensity contours. The RM uncertainties are $<45 \text{ rad m}^{-2}$.

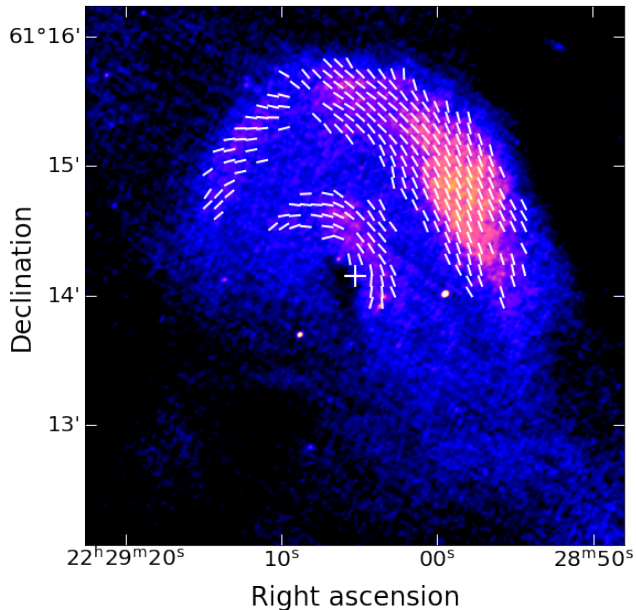


Figure 3. Total intensity map same as Figure 1a, overlaid with unit vectors that show the intrinsic B -field orientation after corrected for Faraday rotation. The vectors are only plotted for regions with Stokes I signal-to-noise ratio > 3 and PA-fit uncertainty $< 15^\circ$. The white cross marks the position of PSR J2229+6114.

Figure 2 presents the RM map of the nebula. The RM value ranges from -380 to -20 rad m^{-2} across the PWN, and the measurement uncertainties are better than 45 rad m^{-2} . Most region of the PWN has roughly constant RM between -250 and -150 rad m^{-2} . This is consistent with the values of $\sim -200 \text{ rad m}^{-2}$ and -187 rad m^{-2} previously reported for the nebula and the

pulsar, respectively (R. Kothes et al. 2006; C. Ng et al. 2020). The core, the lobe, and the tongue have slightly different RM values (-230 , -180 , and -160 rad m^{-2} , respectively), but the discrepancy is not significant given the measurement uncertainty.

Figure 3 shows the intrinsic magnetic field orientation ($\text{PA}+90^\circ$) of the Boomerang. We find a highly ordered field structure, compatible with the large PF observed. The B -field in the core has a toroidal configuration, consistent with previous findings (R. Kothes et al. 2006) and the prediction from the canonical PWN model (C. F. Kennel & F. V. Coroniti 1984; I. Contopoulos et al. 1999). On the other hand, the B -field of the lobe and the tongue are mostly unidirectional. The former well follows the lobe’s elongation, while the latter mainly lies along the east-west direction, misaligned with the elongation of the tongue. The overall magnetic field structure of the lobe and the tongue shows a general toroidal geometry similar to the core but with slight distortion. For example, we would expect the field lines to curve around the northern tip, which is however not observed.

3.3. Spectrum

We measure the flux density of the overall Boomerang PWN from the 6 GHz total intensity map and obtain $80 \pm 30 \text{ mJy}$. The tongue, the lobe, and the core have flux densities of 7 ± 3 , 30 ± 10 , and $9 \pm 3 \text{ mJy}$, respectively. Here we report a rather conservative uncertainty of $\sim 30\%$, due to a highly non-uniform background affected by sidelobes. This is because the observations are only sensitive to angular scales $\lesssim 4'$, comparable to the size of the Boomerang. Adding so the issue is that some short baselines are affected by severe RFI and hence are flagged. All these made the deconvolution process difficult. For this reason, we did not attempt to derive the in-band spectral index from our data. Instead, we estimate the spectral index using tomography. Figure 4 shows the tomography images with a few representative α_t . The core and the lobe show a flat spectrum with an index $\alpha \approx -0.5$, but the tongue and the northwestern edge of the lobe have steeper spectrum of $\alpha \approx -1.0$ and -1.5 , respectively. Note that these estimates could be subject to large uncertainties of $\Delta\alpha \sim 0.2$.

4. DISCUSSION

4.1. PWN structure

Our VLA observations discover new radio features of the Boomerang PWN, including the core, the lobe, and the tongue. The core shows radially decreasing surface brightness. This reflects decreasing magnetic field strength or particle density when the post-shock wind

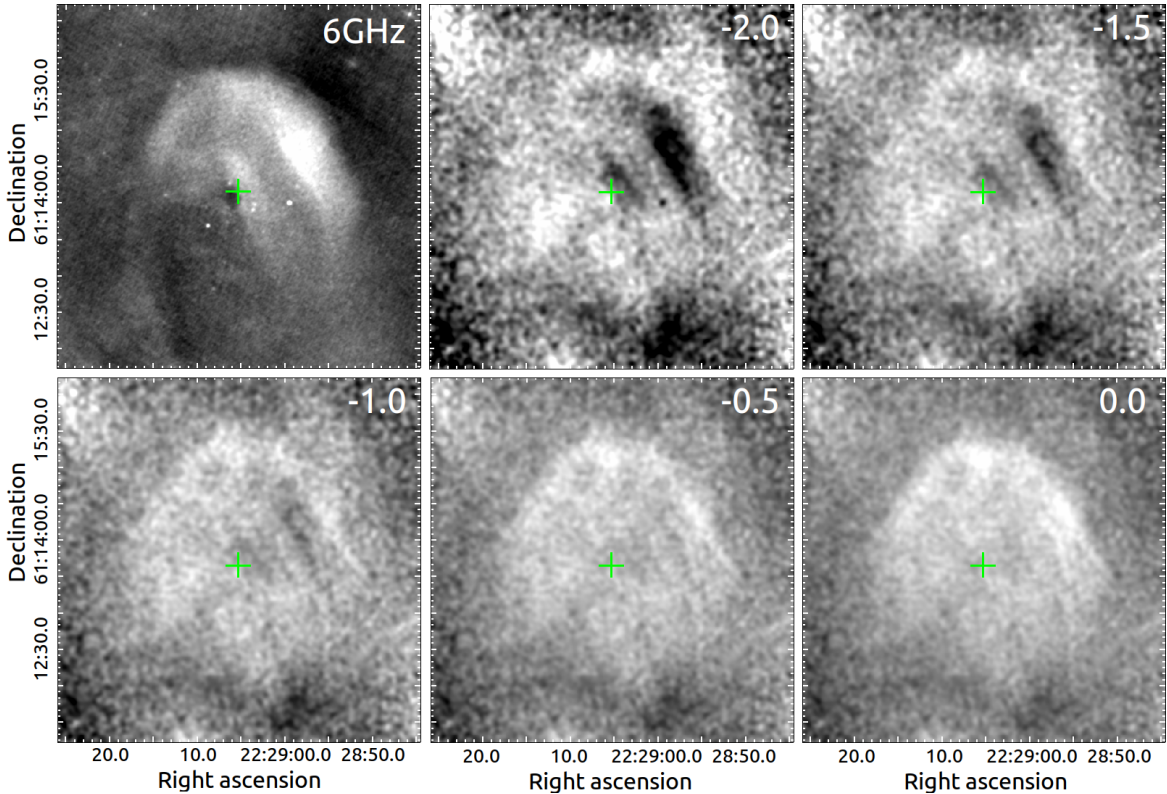


Figure 4. Selected spectral tomography images for the Boomerang between the 4.5 GHz and 7.5 GHz subband total intensity images. The top left panel shows the full band intensity image as Fig. 1a to illustrate the PWN features. For other panels, the trial spectral index α_t is labeled in top right. The cross marks the position of PSR J2229+6114.

transports outwards in a diffusive manner, as observed in X-rays (X.-H. Liang et al. 2022). The outer arc, which consists of the lobe and the tongue, was previously only detected at 1.42 GHz but not at higher frequencies (R. Kothes et al. 2006). Our observations with better sensitivity clearly show its emission up to at least 6 GHz.

If we consider the core as the termination shock, then the radio emission of the Boomerang forms a double tori/arc structure similar to some X-ray PWNe, including the Crab and MSH 15–52 (M. C. Weisskopf et al. 2000; B. M. Gaensler et al. 2002). The outer arc of the Boomerang has a radius of 0.3 pc ($80''$ at 0.8 kpc) comparable to the outer torus of the Crab of 0.4 pc radius (C. Y. Ng & R. W. Romani 2004; R. Lin et al. 2023). Magnetohydrodynamic simulations suggest that such a feature could represent bending of the postshock flow from the pulsar equatorial plane towards the spin axis, due to magnetic hoop stress and slowing down of the flow (S. S. Komissarov & Y. E. Lyubarsky 2003; L. Del Zanna et al. 2006; O. Porth et al. 2014). The compression enhances the particle density and B -field strength, hence forming a toroidal feature. However, we note that this is rarely seen in radio PWNe (e.g., the Crab and 3C 58; N. Bucciantini et al. 2025; C. C. Lang et al. 2010). For young sources, the radio structure could be disrupted by

Rayleigh-Taylor instability from the pulsar wind interaction with the surrounding medium (R. A. Chevalier & S. P. Reynolds 2011). The Boomerang is believed to be a reborn PWN after the passage of the supernova reverse shock, similar to the Vela PWN (R. Kothes et al. 2006). The high pressure environment could suppress the instabilities, such that these two PWNe both exhibit toroidal morphology in radio (R. A. Chevalier & S. P. Reynolds 2011). In addition, our high resolution radio map found no filamentary structure in the Boomerang, adding support to the lack of instabilities. A thick torus model has been developed to explain the torodial structure of radio PWNe, and it was shown that different flow structure, viewing angle, and ambient pressure gradient can produce different PWN morphologies, from a one-sided arc to two-lobe morphology with asymmetrical brightness (R. A. Chevalier & S. P. Reynolds 2011; Y. H. Liu et al. 2023).

Alternatively, the lobe could be caused by the interaction between the pulsar wind and a dense cloud in the surrounding. Previous radio observations found an HI shell engulfing the Boomerang in the north, and the pulsar wind is directly interacting with the cloud (R. Kothes et al. 2001). In this scenario, the shock wave drives a shell in the cloud and accelerates high energy protons

that can give rise to the observed gamma-ray emission (C. Ge et al. 2021). The shock can also reaccelerate the pulsar wind to form the outer arc. This picture gains some support from our polarization results, as we found that the lobe has B -field generally parallel to its elongation, i.e. the shock front. This is similar to some young supernova remnants (e.g., R. Ferrazzoli et al. 2024), and is suggested to be the result of shock compression.

Finally, the non-detection of PSR J2229+6114 in our 6 GHz data is not unexpected. At lower frequencies it has phase-averaged flux densities of 1.5 ± 0.1 mJy and 0.25 ± 0.08 mJy at 350 MHz and 1412 MHz, respectively (J. P. Halpern et al. 2001; K. Stovall et al. 2014). These give a spectral index of 1.3 ± 0.3 . An extrapolation to 6 GHz with a simple power-law suggests 20 ± 10 μ Jy, which is comparable with the noise level of our image. The actual flux density could be lower if there is any spectral turnover between 1–6 GHz, as those gigahertz-peaked pulsars (J. Kijak et al. 2021).

4.2. Magnetic Field

There is a previous claim that the Boomerang has radially increasing RM distribution, and a radial B -field geometry was proposed (R. Kothes et al. 2006). Our high resolution RM map found no evidence for such RM variation (Fig. 2). We suspect that the large beam size in the previous work ($1'15$) could lead to artificial features because of the complex interplay between the field geometry, the source brightness, and the external Faraday dispersion. Moreover, a radial field would result in very faint emission at the center due to the small viewing angle. This is clearly incompatible with the intensity map in Fig. 1. Our result prefers a toroidal field instead. It well explains the polarization structure seen the core (see Fig. 3). For the lobe and the tongue, the B -field is mostly toroidal, albeit with slight distortion that could possibly be due to environmental effects.

Our new study finds very high PF for the Boomerang. In particular, the lobe has intrinsic PF of 67% after accounting for the $\sim 7\%$ bandwidth depolarization. This is very close to the theoretical maximum of $\sim 70\%$ for synchrotron radiation⁵, indicating a highly ordered B -field with negligible depolarization. To compare with PF measured at other frequencies in previous study, we smoothed our Stokes I, Q, and U maps to lower resolution to determine the beam depolarization effect, assuming that the relative brightness between different regions remains the same across frequency bands. The PF val-

Table 2. PF of the Boomerang PWN at different frequencies, from our new data and previously reported values (R. Kothes et al. 2006). The last column lists the PF values after correction for the beam depolarization effect.

Freq. (GHz)	resolution	measured PF	corrected PF
This work			
6	$\sim 2''$	$67 \pm 11\%$	$67 \pm 11\%$
Previous observations			
1.42	$50''$	$31 \pm 5\%$	$33 \pm 5\%$
4.85	$147''$	$37 \pm 5\%$	$62 \pm 8\%$
8.35	$84''$	$52 \pm 5\%$	$64 \pm 6\%$
10.45	$69''$	$50 \pm 6\%$	$57 \pm 7\%$

ues after correction are listed in Table 2. They are all near the synchrotron limit at 4.85, 8.35, and 10.45 GHz, except at 1.42 GHz which is only 33%. These are plotted versus the square of wavelength in Figure 5.

The low PF at 1.42 GHz cannot be attributed to bandwidth depolarization, since the observations have small bandwidth of 10–50 MHz (P. Reich et al. 1997; J. J. Condon et al. 1998; R. Kothes et al. 2001), which can induce at most 6% depolarization for $\text{RM} = -200$ rad m^{-2} . We therefore believe that this is due to Faraday effect, either non-uniform RM in the foreground (i.e. external Faraday dispersion) or Faraday rotation within the PWN. The former effect can be estimated by

$$\text{PF} = \text{PF}_{\text{max}} e^{-2\sigma_{\text{RM}}^2 \lambda^4}, \quad (1)$$

where σ_{RM} is the standard deviation of the RM values within an observing beam (B. J. Burn 1966; D. Farnsworth et al. 2011). Comparing the observed PF of 33% at 1.42 GHz with $\text{PF}_{\text{max}} = 67\%$ implies $\sigma_{\text{RM}} \approx 13$ rad m^{-2} . We derived in Appendix A that if the turbulence in the magnetic field follow the Kolmogorov model, then its characteristic strength $B_{\text{ran}}[\mu\text{G}] \approx 2\sigma_{\text{RM}}[\text{rad m}^{-2}]$ for the observation beam size of $50''$. This requires $B_{\text{ran}} \approx 26$ μG in the interstellar medium (ISM) along the line of sight, much higher than the typical values of a few μG . We therefore conclude that this scenario is rather unlikely. Note that our high resolution RM map has too large uncertainty (45 rad m^{-2}) for σ_{RM} estimate. Better measurements are needed to determine the true value of σ_{RM} from observation.

We next discuss the case that the PWN medium is Faraday thick, such that depolarization is caused by Faraday rotation within the emission volume. Here we focus on the lobe only as it dominates the observed flux. We model it as a Burn slab in the plane of the sky with uniform emissivity, density, and magnetic field (B. J.

⁵ For synchrotron radiation, the maximum PF depends on the spectral index α as $\text{PF} = (1 + \alpha)/(5/3 + \alpha)$. Adopting $\alpha = 0.59$ (R. Kothes et al. 2006) gives $\text{PF} \approx 70\%$.

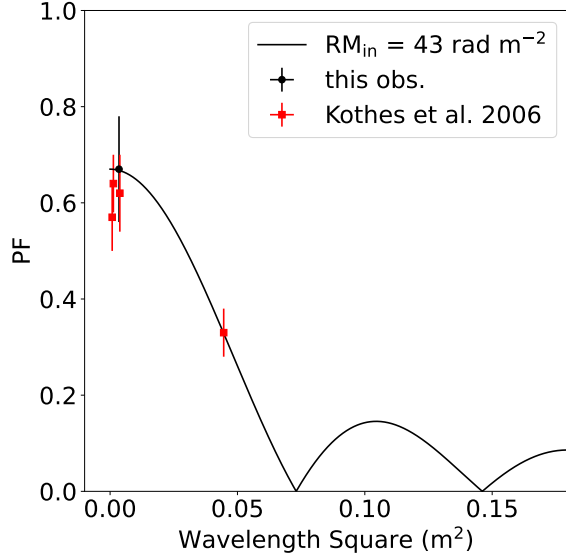


Figure 5. Observed PF versus the square of wavelength. The R. Kothes et al. (2006) data points are corrected for beam depolarization and the line shows the best-fit Burn slab model with $|\text{RM}_{\text{in}}| = 43 \text{ rad m}^{-2}$.

Burn 1966). The observed PF is given by

$$\text{PF} = \text{PF}_{\text{max}} \left| \frac{\sin(\lambda^2 \text{RM}_{\text{in}})}{\lambda^2 \text{RM}_{\text{in}}} \right|, \quad (2)$$

where λ is the observation wavelength and RM_{in} is the equivalent RM if the slab acts as a foreground Faraday screen (B. J. Burn 1966). Taking $\text{PF}_{\text{max}} = 67\%$, $|\text{RM}_{\text{in}}| \approx 43 \text{ rad m}^{-2}$ is needed to explain the PF of 33% at 1.42 GHz. This is illustrated in Figure 5.

The internal RM depends on the slab thickness l , the magnetic field strength along the line of sight $B \cos \theta$, and the cold electrons density $n_{e,\text{cold}}$ as

$$\text{RM}_{\text{in}} \approx 0.812 n_{e,\text{cold}} B l \cos \theta. \quad (3)$$

We ignore relativistic electrons since they contribute very little to the Faraday rotation (T. W. Jones & S. L. Odell 1977). B can be estimated with the standard equipartition assumption

$$B_{\text{eq}} = [6\pi c_{12}(1+k)L\Phi^{-1}V^{-1}]^{2/7} (\sin \theta)^{-3/7}, \quad (4)$$

where c_{12} is a constant (A. G. Pacholczyk 1970; F. Govoni & L. Feretti 2004). We assume the ion-to-electron energy ratio $k = 0$ and the volume filling factor $\Phi = 1$. Using our observed flux density and spectral index of the lobe, we obtain synchrotron luminosity $L \approx 3.5 \times 10^{33} d_{0.8}^2 \text{ erg s}^{-1}$, assuming the emission is in the range 6×10^9 to 10^{18} Hz (X.-H. Liang et al. 2022) at the distance $d = 0.8 d_{0.8} \text{ kpc}$. We take $l = 0.2 \text{ pc}$, same

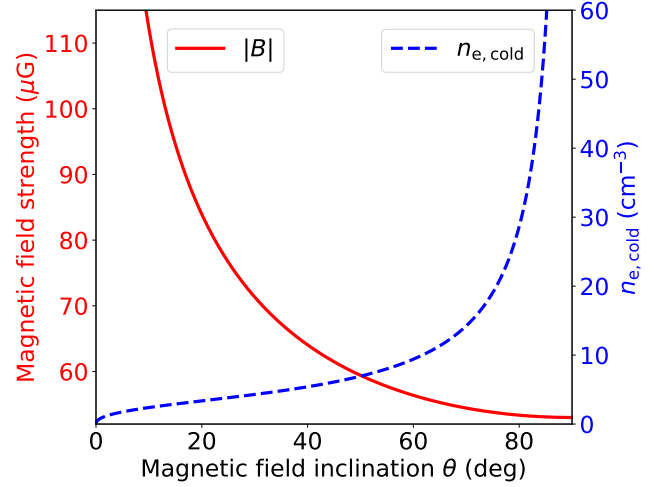


Figure 6. Estimated magnetic field strength (red line) and cold electron density (blue line) of the lobe for different inclination angles between the field and the line of sight.

as the width of the lobe. This gives the emission volume $V \approx 6 \times 10^{53} d_{0.8}^3 \text{ cm}^3$, and hence

$$B_{\text{eq}} \approx 53 (\sin \theta)^{-3/7} d_{0.8}^{-2/7} \mu\text{G} \quad (5)$$

and

$$n_{e,\text{cold}} \approx 5.0 (\sin \theta)^{3/7} (\cos \theta)^{-1} d_{0.8}^{-5/7} \text{ cm}^{-3}. \quad (6)$$

Figure 6 shows the dependence of B and $n_{e,\text{cold}}$ on the viewing angle θ between the field and the line of sight, generated by Eqs. 5 and 6 above. For random B -field orientation, there is 90% chance that θ is between 10° and 85° . This corresponds to field strength approximately between 50 and $105 \mu\text{G}$ and electron density of 2 to 60 cm^{-3} . The former is compatible with estimates from previous study (e.g., X.-H. Liang et al. 2022; I. Pope et al. 2024), and the latter is feasible if the pulsar wind is mixing with the nearby HI cloud. Note that these values weakly depend on the distance. A larger $d = 7.5 \text{ kpc}$ (A. A. Abdo et al. 2009; I. Pope et al. 2024) gives slightly lower B (30–55 μG) and lower $n_{e,\text{cold}}$ (0.5–12 cm^{-3}).

We could further narrow down the range of θ if we assume that the large-scale magnetic field is toroidal following the X-ray torus orientation. The latter has an inclination angle of 46° and the projected axis has position angle of 77° (north through east) (C. Y. Ng & R. W. Romani 2004). Consider the peak emission of the lobe which is at a position angle of $50 \pm 10^\circ$ from the pulsar, the local B -field direction has inclination angle of $\theta = 65 \pm 8^\circ$. Combining with the modelling result,

⁶ $\cos \theta = \sin \theta' \sin i$, where θ' is the position angle of the lobe on the equatorial plane of the torus, $i = 46^\circ$ is the torus inclination

the magnetic field strength of the lobe is $56 \pm 2 \mu\text{G}$, and the electron density $n_e = 12 \pm 4 \text{ cm}^{-3}$.

5. CONCLUSION

We present a high resolution radio study of the Boomerang using VLA observations at 6 GHz. We discover that the radio PWN consists of a compact core surrounding the pulsar and a bright lobe with a tongue. The latter two form an outer arc of $\sim 2'$ diameter. Such structure is rather uncommon among PWNe. We suggest that the arc could be either intrinsic due to the flow structure, or due to the environment, either interaction with the supernova reverse shock or with the surrounding dense cloud. Our polarization measurement reveals a nebular B -field that is mostly toroidal, consistent with what conventional theories predict. We also find a high PF at 6 GHz close to the synchrotron limit, implying a highly ordered B -field structure. On the other hand, the PF at 1.42 GHz is significantly lower. We attribute the discrepancy to Faraday rotation within the emission

volume. This allows us to constrain the B -field to be within 50 to 105 μG . If we further assume that the lobe is part of a toroidal structure, then we can infer a field strength of $\sim 56 \mu\text{G}$.

ACKNOWLEDGMENTS

We thank Roland Kothes for providing us the data of their previous observations on the Boomerang PWN. PCWL is supported by a UCL Graduate Research Scholarship and a UCL Overseas Research Scholarship. C.-Y. N. and S. Zhang are supported by GRF grants of the Hong Kong Government under HKU 7301723 and HKU 17304524. The National Radio Astronomy Observatory is a facility of the National Science Foundation operated under cooperative agreement by Associated Universities, Inc.

Facilities: VLA

Software: CASA ([CASA Team et al. 2022](#))

APPENDIX

A. EXTERNAL FARADAY DISPERSION

To derive the expected external Faraday dispersion, we first find the suitable RM structure function that describes the Boomerang PWN. The RM structure function is defined as

$$D_{\text{RM}}(\delta\theta) = \langle [\text{RM}(\theta) - \text{RM}(\theta + \delta\theta)]^2 \rangle_{\theta}. \quad (\text{A1})$$

It describes the mean squared difference of RM at two positions given a angular separation of $\delta\theta$.

The RM structure function is derived by [A. H. Minter & S. R. Spangler \(1996\)](#) assuming a turbulent interstellar medium that follows the Kolmogorov model, and we find the values of the parameters following the procedures in [P. C. W. Lai et al. \(2022\)](#). The RM structure

function can be expressed as

$$\begin{aligned} D_{\text{RM}}(\delta\theta) = & \left\{ 251.226 \left[\left(\frac{n_e}{0.1 \text{ cm}^{-3}} \right)^2 \left(\frac{C_B^2}{10^{-13} \text{ m}^{-2/3} \mu\text{G}^2} \right) \right. \right. \\ & + \left. \left(\frac{B_{\parallel}}{\mu\text{G}} \right)^2 \left(\frac{C_n^2}{10^{-3} \text{ m}^{-20/3}} \right) \right] \\ & + 23.043 \left(\frac{C_n^2}{10^{-3} \text{ m}^{-20/3}} \right) \\ & \times \left(\frac{C_B^2}{10^{-13} \text{ m}^{-2/3} \mu\text{G}^2} \right) \left(\frac{l_0}{\text{pc}} \right)^{2/3} \left. \right\} \\ & \times \left(\frac{L}{\text{kpc}} \right)^{8/3} \left(\frac{\delta\theta}{\text{deg}} \right)^{5/3}, \end{aligned} \quad (\text{A2})$$

where n_e is the mean density of the medium, B_{\parallel} is the mean magnetic field strength of the line-of-sight component, L is the distance to the source, l_0 is the outer scale of the Kolmogorov turbulence, C_n^2 and C_B^2 is related to the level of fluctuation in density and magnetic field, respectively ([A. H. Minter & S. R. Spangler 1996](#)). In particular, C_B^2 can be expressed as $C_B^2 = 5.2 B_{\text{ran}}^2 (l_0)^{-2/3} \times 10^{-13} \text{ m}^{-2/3} \mu\text{G}^2$, where B_{ran} is the strength of the random B -field.

From observations of the host pulsar of the Boomerang PWN PSR J2229+6114, we know $\text{DM} = n_e L \approx 205 \text{ pc cm}^{-3}$ ([A. E. McEwen et al. 2020](#)) and $|\text{RM}| \approx$

angle, $\tan \theta_{\text{obs}} = \tan \theta' \cos i$, and θ_{obs} is the observed angle difference between the torus axis and the direction of the lobe.

$0.812 n_e |B_{\parallel}| L = 187 \text{ rad m}^{-2}$ (C. Ng et al. 2020). Given the distance to the Boomerang PWN is $L = 800 \text{ pc}$ (R. Kothes et al. 2001), $n_e \approx 0.26 \text{ cm}^{-3}$ and $|B_{\parallel}| \approx 1.1 \mu\text{G}$. We further adopt $l_0 = 3.6 \text{ pc}$ and $C_n^2 = 10^{-3} \text{ m}^{-20/3}$ as suggested in A. H. Minter & S. R. Spangler (1996). B_{ran} of the interstellar medium varies quite a lot depending on the location, but is in general smaller than $10 \mu\text{G}$ (A. H. Minter & S. R. Spangler 1996; M. Haverkorn et al. 2008). Putting the values back into Eq. A2, we get

$$D_{\text{RM}}(\delta\theta) \approx \left[2.33 \left(\frac{B_{\text{ran}}}{\mu\text{G}} \right)^2 + 0.18 \right] \left(\frac{\delta\theta}{1'} \right)^{5/3} \text{ rad}^2 \text{ m}^{-4}. \quad (\text{A3})$$

Given a circle with angular size r , the expected value of D_{RM} between two randomly selected points within the circle can be expressed as

$$\begin{aligned} \langle D_{\text{RM}} \rangle_r &= \langle (\text{RM}_i - \text{RM}_j)^2 \rangle_r \\ &= 2 \langle \text{RM}^2 \rangle_r - 2 \langle \text{RM} \rangle_r^2 \\ &= 2\sigma_{\text{RM}}^2, \end{aligned} \quad (\text{A4})$$

where σ_{RM} is the standard deviation of RM within a beam that we want to find for Eq. 1. With Eq. A3, we calculate $\langle D_{\text{RM}} \rangle_r$ using Monte Carlo simulation and found $\langle D_{\text{RM}} \rangle_{r=50''} \approx 0.51 B_{\text{ran}}^2$. Therefore, we obtain

$$\sigma_{\text{RM}} [\text{rad m}^{-2}] \approx 0.5 B_{\text{ran}} [\mu\text{G}]. \quad (\text{A5})$$

REFERENCES

- Abdo, A. A., Ackermann, M., Ajello, M., et al. 2009, *ApJ*, 706, 1331, doi: [10.1088/0004-637X/706/2/1331](https://doi.org/10.1088/0004-637X/706/2/1331)
- Amato, E. 2024, arXiv e-prints, arXiv:2402.10912, doi: [10.48550/arXiv.2402.10912](https://doi.org/10.48550/arXiv.2402.10912)
- Bietenholz, M. F., & Kronberg, P. P. 1990, *ApJL*, 357, L13, doi: [10.1086/185755](https://doi.org/10.1086/185755)
- Bucciantini, N., Wong, J., Romani, R. W., et al. 2025, *A&A*, 699, A33, doi: [10.1051/0004-6361/202554216](https://doi.org/10.1051/0004-6361/202554216)
- Burn, B. J. 1966, *MNRAS*, 133, 67, doi: [10.1093/mnras/133.1.67](https://doi.org/10.1093/mnras/133.1.67)
- Cao, Z., Aharonian, F. A., An, Q., et al. 2021, *Nature*, 594, 33, doi: [10.1038/s41586-021-03498-z](https://doi.org/10.1038/s41586-021-03498-z)
- CASA Team, Bean, B., Bhatnagar, S., et al. 2022, *PASP*, 134, 114501, doi: [10.1088/1538-3873/ac9642](https://doi.org/10.1088/1538-3873/ac9642)
- Chevalier, R. A., & Reynolds, S. P. 2011, *ApJL*, 740, L26, doi: [10.1088/2041-8205/740/1/L26](https://doi.org/10.1088/2041-8205/740/1/L26)
- Condon, J. J., Cotton, W. D., Greisen, E. W., et al. 1998, *AJ*, 115, 1693, doi: [10.1086/300337](https://doi.org/10.1086/300337)
- Contopoulos, I., Kazanas, D., & Fendt, C. 1999, *ApJ*, 511, 351, doi: [10.1086/306652](https://doi.org/10.1086/306652)
- Del Zanna, L., Volpi, D., Amato, E., & Bucciantini, N. 2006, *A&A*, 453, 621, doi: [10.1051/0004-6361:20064858](https://doi.org/10.1051/0004-6361:20064858)
- Dodson, R., Lewis, D., McConnell, D., & Deshpande, A. A. 2003, *MNRAS*, 343, 116, doi: [10.1046/j.1365-8711.2003.06653.x](https://doi.org/10.1046/j.1365-8711.2003.06653.x)
- Farnsworth, D., Rudnick, L., & Brown, S. 2011, *AJ*, 141, 191, doi: [10.1088/0004-6256/141/6/191](https://doi.org/10.1088/0004-6256/141/6/191)
- Ferrazzoli, R., Prokhorov, D., Bucciantini, N., et al. 2024, *ApJL*, 967, L38, doi: [10.3847/2041-8213/ad4a68](https://doi.org/10.3847/2041-8213/ad4a68)
- Gaensler, B. M., Arons, J., Kaspi, V. M., et al. 2002, *ApJ*, 569, 878, doi: [10.1086/339354](https://doi.org/10.1086/339354)
- Gaensler, B. M., & Wallace, B. J. 2003, *ApJ*, 594, 326, doi: [10.1086/376861](https://doi.org/10.1086/376861)
- Ge, C., Liu, R.-Y., Niu, S., Chen, Y., & Wang, X.-Y. 2021, *The Innovation*, 2, 100118, doi: [10.1016/j.xinn.2021.100118](https://doi.org/10.1016/j.xinn.2021.100118)
- Govoni, F., & Feretti, L. 2004, *International Journal of Modern Physics D*, 13, 1549, doi: [10.1142/S0218271804005080](https://doi.org/10.1142/S0218271804005080)
- Halpern, J. P., Camilo, F., Gotthelf, E. V., et al. 2001, *ApJL*, 552, L125, doi: [10.1086/320347](https://doi.org/10.1086/320347)
- Haverkorn, M., Brown, J. C., Gaensler, B. M., & McClure-Griffiths, N. M. 2008, *ApJ*, 680, 362, doi: [10.1086/587165](https://doi.org/10.1086/587165)
- Jones, T. W., & Odell, S. L. 1977, *ApJ*, 214, 522, doi: [10.1086/155278](https://doi.org/10.1086/155278)
- Kennel, C. F., & Coroniti, F. V. 1984, *ApJ*, 283, 694, doi: [10.1086/162356](https://doi.org/10.1086/162356)
- Kijak, J., Basu, R., Lewandowski, W., & Rożko, K. 2021, *ApJ*, 923, 211, doi: [10.3847/1538-4357/ac3082](https://doi.org/10.3847/1538-4357/ac3082)
- Komissarov, S. S., & Lyubarsky, Y. E. 2003, *MNRAS*, 344, L93, doi: [10.1046/j.1365-8711.2003.07097.x](https://doi.org/10.1046/j.1365-8711.2003.07097.x)
- Kothes, R., Landecker, T. L., Reich, W., Safi-Harb, S., & Arzoumanian, Z. 2008, *ApJ*, 687, 516, doi: [10.1086/591653](https://doi.org/10.1086/591653)
- Kothes, R., Reich, W., & Uyaniker, B. 2006, *ApJ*, 638, 225, doi: [10.1086/498666](https://doi.org/10.1086/498666)
- Kothes, R., Uyaniker, B., & Pineault, S. 2001, *ApJ*, 560, 236, doi: [10.1086/322511](https://doi.org/10.1086/322511)
- Lai, P. C. W., Ng, C. Y., & Bucciantini, N. 2022, *ApJ*, 930, 1, doi: [10.3847/1538-4357/ac63b1](https://doi.org/10.3847/1538-4357/ac63b1)
- Lang, C. C., Wang, Q. D., Lu, F., & Clubb, K. I. 2010, *ApJ*, 709, 1125, doi: [10.1088/0004-637X/709/2/1125](https://doi.org/10.1088/0004-637X/709/2/1125)
- Liang, X.-H., Li, C.-M., Wu, Q.-Z., Pan, J.-S., & Liu, R.-Y. 2022, *Universe*, 8, 547, doi: [10.3390/universe8100547](https://doi.org/10.3390/universe8100547)

- Lin, R., van Kerkwijk, M. H., Kirsten, F., Pen, U.-L., & Deller, A. T. 2023, *ApJ*, 952, 161, doi: [10.3847/1538-4357/acdc98](https://doi.org/10.3847/1538-4357/acdc98)
- Liu, S., Zeng, H., Xin, Y., & Zhu, H. 2020, *ApJL*, 897, L34, doi: [10.3847/2041-8213/ab9ff2](https://doi.org/10.3847/2041-8213/ab9ff2)
- Liu, Y. H., Ng, C. Y., & Dodson, R. 2023, *ApJ*, 945, 82, doi: [10.3847/1538-4357/acb20d](https://doi.org/10.3847/1538-4357/acb20d)
- Ma, Y. K., Ng, C. Y., Bucciantini, N., et al. 2016, *ApJ*, 820, 100, doi: [10.3847/0004-637X/820/2/100](https://doi.org/10.3847/0004-637X/820/2/100)
- McEwen, A. E., Spiewak, R., Swiggum, J. K., et al. 2020, *ApJ*, 892, 76, doi: [10.3847/1538-4357/ab75e2](https://doi.org/10.3847/1538-4357/ab75e2)
- Minter, A. H., & Spangler, S. R. 1996, *ApJ*, 458, 194, doi: [10.1086/176803](https://doi.org/10.1086/176803)
- Ng, C., Pandhi, A., Naidu, A., et al. 2020, *MNRAS*, 496, 2836, doi: [10.1093/mnras/staa1658](https://doi.org/10.1093/mnras/staa1658)
- Ng, C. Y., & Romani, R. W. 2004, *ApJ*, 601, 479, doi: [10.1086/380486](https://doi.org/10.1086/380486)
- Ng, C. Y., & Romani, R. W. 2008, *ApJ*, 673, 411, doi: [10.1086/523935](https://doi.org/10.1086/523935)
- Olmi, B., & Bucciantini, N. 2023, *PASA*, 40, e007, doi: [10.1017/pasa.2023.5](https://doi.org/10.1017/pasa.2023.5)
- Olmi, B., Del Zanna, L., Amato, E., Bucciantini, N., & Mignone, A. 2016, *Journal of Plasma Physics*, 82, 635820601, doi: [10.1017/S0022377816000957](https://doi.org/10.1017/S0022377816000957)
- Pacholczyk, A. G. 1970, *Radio astrophysics. Nonthermal Processes in Galactic and Extragalactic Sources* (San Francisco, CA: Freeman)
- Pope, I., Mori, K., Abdelmaguid, M., et al. 2024, *ApJ*, 960, 75, doi: [10.3847/1538-4357/ad0120](https://doi.org/10.3847/1538-4357/ad0120)
- Porth, O., Komissarov, S. S., & Keppens, R. 2014, *MNRAS*, 438, 278, doi: [10.1093/mnras/stt2176](https://doi.org/10.1093/mnras/stt2176)
- Reich, P., Reich, W., & Furst, E. 1997, *A&AS*, 126, 413, doi: [10.1051/aas:1997274](https://doi.org/10.1051/aas:1997274)
- Reich, W. 2002, in *Neutron Stars, Pulsars, and Supernova Remnants*, ed. W. Becker, H. Lesch, & J. Trümper, 1. <https://arxiv.org/abs/astro-ph/0208498>
- Stovall, K., Lynch, R. S., Ransom, S. M., et al. 2014, *ApJ*, 791, 67, doi: [10.1088/0004-637X/791/1/67](https://doi.org/10.1088/0004-637X/791/1/67)
- Wardle, J. F. C., & Kronberg, P. P. 1974, *ApJ*, 194, 249, doi: [10.1086/153240](https://doi.org/10.1086/153240)
- Weisskopf, M. C., Hester, J. J., Tennant, A. F., et al. 2000, *ApJL*, 536, L81, doi: [10.1086/312733](https://doi.org/10.1086/312733)
- Yang, C., Zeng, H., Bao, B., & Zhang, L. 2022, *A&A*, 658, A60, doi: [10.1051/0004-6361/202141850](https://doi.org/10.1051/0004-6361/202141850)